Measurement of the Ion Blocking by the Passive Bipolar Grid

Evgeny Shulga, Vladislav Zakharov, Prakhar Garg, Thomas K. Hemmick, and Alexander Milov

***Abstract*— The ion backflow (IBF) is the main limiting factor for operating time projection chambers (TPCs) at high event rates. A significant effort is invested by many experimental groups to solve this problem. This article explores a solution based on operating a passive bipolar wire grid. In the presence of the magnetic field, the grid more effectively attenuates the ion current than the electron current going through it. Transparencies of the grid to electrons and ions are measured for different gas mixtures and magnitudes of the magnetic field. The results suggest that in a sufficiently strong magnetic field, the bipolar wire grid can be used as an effective and independent device to suppress the IBF in TPCs.**

***Index Terms*— Gaseous detector, gas electron multiplier (GEM), ion backflow (IBF) suppression, time projection chamber (TPC).**

I. Introduction

THE time projection chambers (TPCs) are introduced by Nygren [1] and have been successfully used in different particle physics experiments [2]–[8]. TPCs have a number of features that make them an attractive technological choice for detectors in high-energy and nuclear physics experiments.

Due to their excellent capability to reconstruct 3-D topology of charged particles produced in interactions, TPCs are widely used in experiments where the measurement of a multiparticle final state is required. Being operated in an external magnetic field, TPCs provide high-precision momentum measurement of the tracks, down to very low magnitudes. Sampling energy deposition in the gas working volume gives TPCs the particle identification capabilities. The use of the gas as a working medium makes TPCs a low-radiation length detectors that are easily combined with detectors based on other technologies as it is required in most modern experiments. Last but not least, TPCs are relatively inexpensive devices. A combination of these features makes TPCs a widely used detector technology after more than 45 years since it was introduced.

Together with the advantages, the main setback of TPCs is the low data-taking rate which is a severe constraint on the use of TPCs in modern experiments requiring high data-taking rates. Among several factors that affect the rates, the most difficult to overcome is the space charge that builds up in the TPC volume and distorts the drift of the primary ionization. Charges in the TPC volume are carried by slow-moving ions produced in the readout elements of the TPC. This is known as the positive ion backflow (IBF) problem.

To address the IBF problem, the first TPC built in 1984 [2] used a plane of wires called the bipolar gating grid (BPG) separating TPC readout elements from the drift volume. Applying positive and negative bias voltages to odd and even wires of the grid stops the ion and electron flow through the BPG. TPCs developed in recent years [9]–[11] adopt the concept of amplification element being also the IBF stopper. Multiple-layer micropattern detectors used as amplification elements are capable of trapping ions between their layers [12]–[20]. Nevertheless, most of the large TPCs built nowadays rely on the BPG to suppress the IBF [21].

A BPG can be operated in synchronous and passive modes [22], [23]. The former implies that the voltage bias on the wires is synchronized with an external trigger. The duration and the frequency of pulses ensure that all ions are collected on the BPG. It also results in stopping the electrons going through the BPG, producing a dead time in the system. In the presence of the magnetic field, the voltages required to stop electrons are higher than those that are required to stop the ions, which allows the BPG to retain some electron transparency when the ion current is fully shut. It opens the possibility to operate the BPG in passive mode with constant biases on odd and even wires. Achieving high data-taking rates in a TPC operated in a passive mode is much easier. All TPCs built by the large-particle experiments till date used the BPG in a synchronous mode, although passive mode was also considered for the detectors in the magnetic fields above 1 T [7], [8].

The principle of the BPG operation in a passive mode is based on the effect that in the presence of the magnetic and electric fields, the direction of the electron drift has a component along the vector product of the two fields. The electron drift in this direction is described with the Lorentz angle that is explained in many works [21], [24]–[26] and, therefore, is not elaborated here. This article provides a detailed study of the BPG transparency for electrons and ions in different gas mixtures in the presence of the magnetic field. The results show that the BPG operated in a passive mode can be used as an effective element to suppress the IBF in the

Manuscript received July 27, 2020; revised October 13, 2020; accepted November 21, 2020. Date of publication December 3, 2020; date of current version January 19, 2021. This work was supported by the United States-Israel Binational Science Foundation (BSF), Jerusalem, Israel, under Grant 2016240.

Evgeny Shulga and Alexander Milov are with the Department of Particle Physics and Astrophysics, Weizmann Institute of Science, Rehovot 7610001, Israel (e-mail: evgeny.shulga@weizmann.ac.il).

Vladislav Zakharov, Prakhar Garg, and Thomas K. Hemmick are with the Department of Physics and Astronomy, Stony Brook University, Stony Brook, NY 11794 USA.

Color versions of one or more figures in this article are available at https://doi.org/10.1109/TNS.2020.3042311.

Digital Object Identifier 10.1109/TNS.2020.3042311

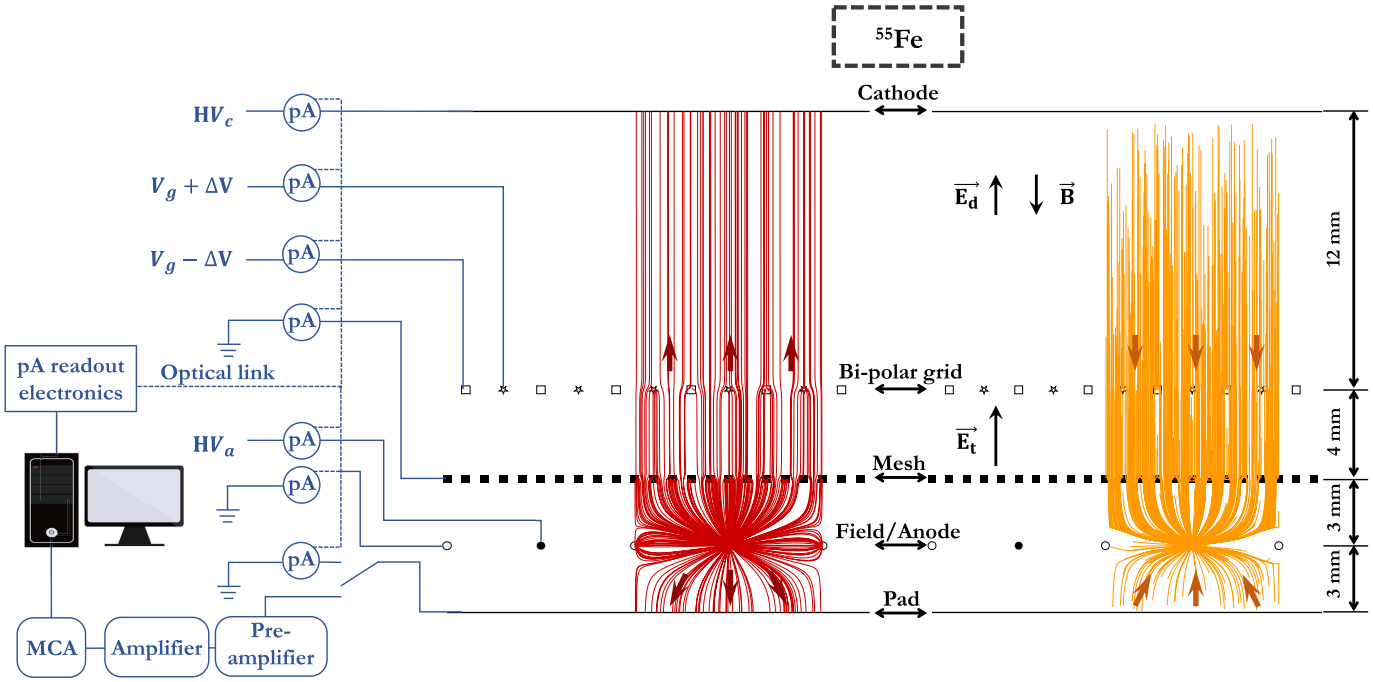

Fig. 1. Schematic view of the experimental setup. Colored (online) lines represent ion (left) and electron (right) drift trajectories, respectively.

TPCs operated in a strong magnetic field, for example, in the sPHENIX TPC [27], [28].

II. Measurements

A. Setup

The setup built at the Weizmann Institute consists of the BPG sandwiched between the ion-generating plane and the ion-receiving cathode immersed into a gas volume. A schematic view of the setup is shown in Fig. 1.

All frames used in the setup have the working area of 27×27 mm^2. The primary ionization is produced by the ^{55}Fe source positioned above the gas volume. At the time of measurement, the source intensity was approximately 3.5 mCi. The amount of gamma radiation illuminating the detector volume is controlled by a collimator.

X-rays from the source enter the gas volume through a cathode electrode built of a thin gas electron multiplier (GEM) electrically connected on both sides and illuminates the entire detector. A volume between the cathode and the BPG has a vertical dimension of 12 mm. Photons converted in this volume produce primary ionization that drifts toward the BPG. The BPG is built of 50 μm wires spaced by 1 mm. Odd and even wires of the BPG are set to a voltage of $V_g \pm \Delta V$ fed on the opposite sides of the frame. Thus, the adjacent wires have a voltage difference of $2\Delta V$. The mesh electrode is located 4 mm below the BPG. It is made of the stainless steel mesh with 0.5×0.5 mm^2 cells and a wire diameter of 50 μm, providing $\sim$80% optical transparency. Electrons passing the BPG and those that are coming from conversions inside the 4-mm space enter the mesh electrode. A collimator (not shown in the figure) that immediately follows the mesh is made of a thin dielectric material and limits the working area of the detector to a circle of 20 mm in diameter. The collimator eliminates the edge effects and increases lateral uniformity of the ionization flux.

The wire plane located 3 mm below the mesh is made of 50-μm Cu/Rh wires spaced by 2.5 mm. Voltages are applied to the wires on opposite sides of the frame. Field wires are grounded and anode wires are set to 1.7–2.1 kV to provide the desired gas gain depending on the gas mixture. To reduce parasitic currents flowing between the field and anode wires, the grooves are made in the FR4 material of the frames holding the wires. Wires and grooves are covered with epoxy. During the assembly, the anode and field wires on the wire plane are directed orthogonally to the BPG wires. This plane is located 3 mm above the pad plane that is grounded. Electrons from the conversion of the ^{55}Fe photons that occur in this volume reach the anode wires without passing through any other element in the setup.

The setup is shown in Fig. 1. It is assembled in a $15 \times 15 \times 3$ cm^3 dielectric box and covered with a copper foil on the outside for electrical grounding. The vertical size of the box is constrained by the dimension of the magnet bore in which the dipole field up to 1.2 T is generated by a magnet produced by Danphysik GGG. The field is controlled by Group3 DTM-151 tesla meter with MPT-141 probe providing 0.012% accuracy.

The HV is supplied by CAEN N471 and Lambda Z^+ 320 power supplies through the low-pass filters with $RC \approx 2$ s. All conductive elements in the setup are read out by the floating picoammeters connected to the computer via optical links. Picoammeters are produced by PicoLogic J.D.O.O. in Zagreb [29]. In the working regime, the parasitic currents in the measured channels averaged over 1 s are

in 5–80 pA range at the highest anode voltages. Signals from the pad electrode can be switched to the charge-measuring channel consisting of the Ortec charge-sensitive preamplifier 142 IH followed by a shaping amplifier Ortec 672 and read out by the Ortec multichannel analyzer (MCA), Ametek Easy-MCA 2000.

The gas mixtures are prepared in a gas-mixing station using calibrated mass flow controllers (Aalborg GFCS). Flow controllers are calibrated by the water displacement method after each change of mixed gases. The accuracy of the quenching fraction in the gas mixture is $\pm 3.5\%$ for (90:10) gas mixtures and $\pm 1.5\%$ for (50:50) gas mixtures. Gas flow is set to provide detector volume exchange every 10 min, preventing possible outgassing from the structural elements of the setup into the working gas atmosphere. The gas used in the measurement comes in the bottles with purity $>99.99\%$ and is not recirculated during the measurements.

B. Definitions of Transparency

The measurements are carried out at a sufficiently high gain on anode wires such that the contribution of the primary ionization to the currents (i) can be neglected. Then

$$-i_a = i_c + i_g + i_m + i_f + i_p \tag{1}$$

is fulfilled with the accuracy of picoammeters. Currents in the equation correspond to cathode (i_c), BPG (i_g), mesh (i_m), field (i_f), pad (i_p), anode (i_a) electrodes, respectively, as shown in Fig. 1.

The BPG is considered here as a standalone element in an arbitrary TPC detector. For electrons and ions traversing the BPG, its impact can be characterized by transparency parameters denoted as T_e^g and T_i^g, respectively. From the setup shown in Fig. 1 and (1)

$$T_i^g = \frac{i_c}{-i_a - i_p - i_m - i_f}. \tag{2}$$

That is, the ion current reaching the cathode above the BPG divided by the ion current that flows into the BPG, that is, the ion current emerging from the anode wires is less than the currents in pad, field, and mesh electrodes. Analogously, one can also define the ion transparency of the mesh electrode

$$T_i^m = \frac{i_c + i_g}{-i_a - i_p - i_f}. \tag{3}$$

T_e^g cannot be defined as a ratio of currents, because the electron components in all currents, except in i_a, are negligibly small. The value of i_a depends on the amount of initial ionization in all parts of the setup. Neglecting electron attachment, electrons from photon conversions in the gas arrive at anode wires unless they are captured by the BPG or the mesh. By changing ΔV on BPG, one can suppress or fully block electrons coming from the detector volume above the BPG. This consideration leads to (4) which is the ratio of the anode current, coming from everywhere in the setup, to the current that is coming from below the BPG. T_e^g can be deduced from the shape of i_a measured as a function of ΔV:

$$\frac{i_a(\Delta V)}{i_a(E_d = 0)} = 1 + K T_e^m T_e^g(\Delta V). \tag{4}$$

The constant coefficient of K in the equation is a relative amount of primary ionization that is generated above and below the BPG and amplified on the anode wires. T_e^m is the mesh transparency to electrons. To first order, these coefficients do not depend on ΔV since the electric fields around the mesh are not affected by the voltages between the BPG wires (see Fig. 1).

The anode current on the left-hand side of the equation is divided by the current, measured when electrons from above are not flowing to the BPG, $i_a(E_d = 0)$. It is experimentally proved that the same current is measured in the anode wires when the BPG is fully closed to primary electrons. In this case, the reduced i_a is equal to unity. Thus, the shape of the T_e^g dependence can be extracted from measuring $i_a(\Delta V)$ and using (4). Determining the absolute normalization of T_e^g from (4) requires precise knowledge of the coefficient K, which in turn depends on the geometry of all elements in the setup. Instead, for the final results, the absolute normalization of T_e^g was worked out as follows.

Charge distributions from the ^{55}Fe ionization source are measured in the pad electrode for three different cases: ionization that is coming to the anode directly; ionization reaching the anode through the mesh; ionization reaching anode through mesh and BPG. These distributions are obtained by setting the drift field (E_d) between the cathode and the BPG and the transfer field (E_t) between the BPG and the mesh to their nominal values or zero. The three distributions are shown with lines in the left panel of Fig. 2, the corresponding field settings are mentioned in the figure legend. Primary ionization from the photons converting above the BPG drifts through the BPG and the mesh and, therefore, is attenuated by the factor (T_e^g T_e^m). Primary ionization from the photons converted between the BPG and the mesh is attenuated by the factor of T_e^m only. Therefore, by subtracting distributions, one can compare two distributions before and after the BPG. The ratio of the mean values of these two distributions after extrapolating them to zero provides the absolute normalization of T_e^g. The right panel of Fig. 2 shows the result of this measurement with filled markers. The results are compared to the current measurement based on (4) and shown with open markers. All points in the current measurement are multiplied by the same factor such that the first point, at $\Delta V = 0$, gets the value of the charge measurement. After this, both curves agree in the region $\Delta V < 20$ V. Above 20 V, the charge measurement becomes difficult because peaks shown in the left panel of the figure disappear and distributions shift close to zero values. Results presented in this article are based on the measurement deduced from the currents and normalized from the charges.

C. Source Intensity

The amount of ionization let into the system by the collimator is chosen as a compromise. Lowering currents to a few powerampare requires extension of the measurement cycle to hours and makes smaller effects enter the consideration such as control over detector stability, better knowledge of the baseline values, additional control over low-frequency microdischarges,

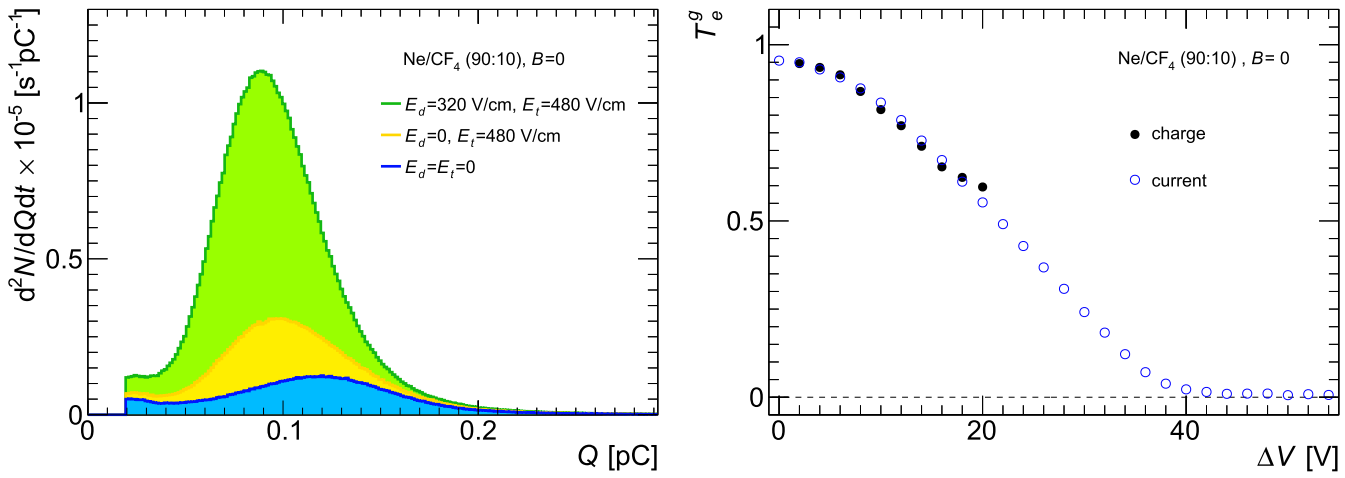

Fig. 2. Left: charge distributions measured in the pad electrode at different field configurations. Right: T_e^g as a function of ΔV calculated from the currents and the charge measurements. The magnitude of the current measurement at $\Delta V = 0$ is set to the value of the charge measurement and therefore is not shown.

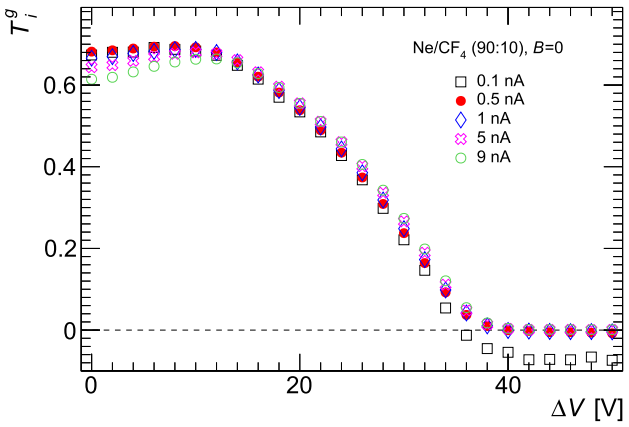

Fig. 3. T_i^g as a function of ΔV measured using different current ranges indicated with i_c ($\Delta V = 0$) in the legend.

and so on. Increasing the currents results in the build-up of the space charge in the setup that alters electric fields around the BPG. Although the space charge problem is typically associated with much larger detectors, the setup is shown in Fig. 1 with the working area of approximately 3 cm^2 and relatively short gaps operates at much higher current densities than most of the larger detectors.

The space charge effects are studied with the T_i^g curve measured with different currents. It is done by attenuating the ^{55}Fe source with the collimator and by lowering the gas gain. The results are shown in Fig. 3. Current ranges are characterized by the cathode current $i_c(\Delta V = 0)$, typically the largest current used to produce the corresponding curve. The study shows that the measurements made with currents below 500 pA are hard to reproduce and are considered unstable, whereas in the range above 1 nA the space-charge effects start to develop at $\Delta V = 0$. Thus, for the results presented in this article, the currents in the cathode are kept below 1 nA to avoid space-charge effects and prevent zero-current miss-measurement.

D. Measurement Procedure

1) General Settings: All measurements follow the standard procedure. The gas flow is set to approximately 30 cm^3/min and the detector is flushed over 1 h, corresponding to more than ten detector and tubing volume exchanges. The magnetic field is set to the desired value. Voltages are set on anode, cathode, and both types of the BPG wires. Pad, field, and mesh electrodes remain grounded. The gas gain is set to the nominal value of 3500 measured by the position of the ionization peak in the pad. The collimator is adjusted to produce the i_c current from the ^{55}Fe source close to 1 nA. The detector is operated in this stage for approximately 30 min after which the settings are additionally adjusted if needed.

The following three measurements are performed in each gas mixture at each magnetic field magnitude and combined to produce the final results reported in this article.

2) Transfer Field Scan: The BPG transparency to ions and electrons strongly depends on the magnitudes of E_d and E_t, which choice is closely related to properties of gas and many other considerations [8], [30], including the Lorentz angle. Since optimization of the gas mixture and E_d is not feasible in the scope of this article, to make comparative studies of the BPG performance, different gases are measured in the same field configuration, called "main" in which E_d is kept at a constant value of 320 V/cm in all measurements. To find dependence on E_t, the voltages on cathode and BPG are set to values that provide $E_d = 320$ V/cm and $E_t = 0.5E_d = 160$ V/cm. The two voltages are then increased in steps such that E_t is incremented by $0.125E_d$ until it reaches $2.5E_d$. After each voltage change, the detector is operated for a waiting time of 5 min without any change and then the measurement is taken averaged over 1 min.

Results of the E_t scan are shown in Fig. 4. The electron transparency curve T_e shown with circles is the product of $(T_e^g T_e^m)$. Since the electric field below mesh is defined by the voltage on the anode wires and is much stronger than E_t, T_e^m is high and, therefore, does not strongly depend on E_t, as long

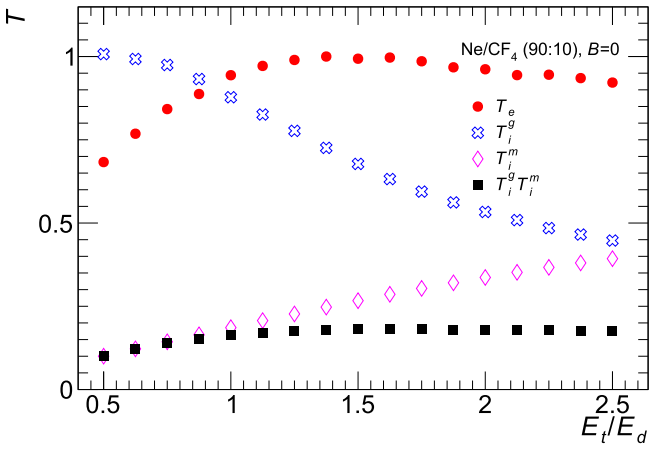

Fig. 4. Transparencies as a function of E_t/E_d scan for $E_d = 320$ V/cm. T_e is the product of $T_e^g T_e^m$ normalized to unity at maximum.

as E_t is low. A small decrease in T_e above $Et/Ed > 1.5$ seen in the figure may indicate a departure from this regime. T_e increases with increasing E_t and reaches a maximum around $E_t = 1.5E_d$. T_i^g, shown with crosses, steadily decreases with increasing E_t. This, however, is offset by an increase of T_i^m shown in the plot with diamonds. Analogous effects would also be present in a real detector in which E_t coupled to the TPC amplification plane below the BPG would extract ions into the drift volume of the detector. Those two effects nearly cancel each other above $E_t = E_d$ as shown in Fig. 4 with square symbols, which are the product of (T_i^g T_i^m).

As a result of this study, the working setting is chosen $w = E_t/E_d = 1.5$, $E_t = 480$ V/cm. Since the result measured in different gases are comparable, and following the decision to use the constant E_d, the same E_t value is used in all measurements to facilitate comparisons between different gas mixtures.

3) Charge Measurement: The pad electrode is connected to the charge measurement line. To minimize the MCA dead time <5%, the collimator is adjusted to provide the counting rate in the detector below 10^5 s^{-1}. Three measurements are taken with fields set to

1) $E_t = E_d = 0$.
2) $E_d = 0$, $E_t = 480$ V/cm.
3) $E_d = 320$ V/cm, $E_t = 480$ V/cm.

Data-taking time for each measurement is 5 min, and the measurements are done to collect sufficient statistics. The results of this measurement are shown in the left panel of Fig. 2 and are used for absolute normalization of T_e^g.

4) BPG Voltage Scan: For this measurement, a pad electrode is reconnected to the picoammeter, cathode and BPG are kept at the setting as for the last measurement in Section II-D.3, and the collimator is returned to its previous setting. The measurements are taken for ΔV increasing from 0 to 80 V in 2-V increments. The picoammeters values are averaged over 60 s time after 10 s waiting time following each change in the voltage settings. Results of this measurement for T_e^g are shown in the right panel of Fig. 2 and for T_i^g in Fig. 3.

III. Uncertainties of the Measurements

The nominal accuracy of the devices used in the measurement plays little role in the final results. These include precision of the power supplies, gas flow controllers, magnet, measuring devices, and so on.

The mechanical tolerance of the setup assembly is within hundreds of micrometers so that the fields discussed in the article are known with a typical accuracy of 5%. The nonuniformity of the gas gain, wire spacing, and impact of the field distortion at the edges was studied by changing the illumination angle of the collimator radiation while keeping a similar counting rate. An approximate 2% difference was found in the result which is assigned to the uncertainties.

Detector stability was estimated to contribute up to 5% uncertainty which is the difference between two identical measurements performed with a month interval during which the detector was reassembled and the gas mixture was changed more than once.

Possible residual space-charge effects in the measurements performed with the currents $i_c < 1$ nA are estimated as 10% of the difference between the measurements done at $i_c = 10$ nA and $i_c = 1$ nA. They contribute up to 2% at the highest i_c in the measurement of T_i^g.

The absolute normalization of the T_e^g curve explained in Section II-D.3 relies on the extrapolation of the curves shown in Fig. 2 to zero values. A 3% uncertainty is added to the result based on the uncertainties in extrapolation.

As follows from the setup shown in Fig. 1, applying ΔV to BPG shall not affect the mesh transparencies as long as the average BPG potential remains the same. However, a small change up to 7% of the measured T_i^m value given by (3) is observed in the experiment. This value is directly assigned to the T_i^g as an uncertainty.

The contribution of different sources depends on ΔV. At the highest transparency values, the uncertainties reach 7.5%. At the transparency values close to zero, the systematic uncertainty remains at the level of 0.5% of the full scale and is approximately symmetric around zero, reflecting the fact that the results are obtained by subtracting measured currents as explained in Section II. The uncertainties of T_e^g and T_i^g are not the same, but are close in their values and are partially correlated with each other. To preserve the clarity of the plots, the dependence of systematic uncertainty on ΔV is shown as a band around zero. It has to be taken as the uncertainty estimator for individual curves shown in figures.

IV. Results

The BPG transparencies in the Ne:CF$_4$ (90:10) gas mixture are shown in Fig. 5. Results for other gas mixtures are given in the Appendix. Measurements are done with the magnetic field switched off and at the values 0.4, 0.8, and 1.2 T. T_e^g and T_i^g are denoted by closed and open markers, respectively. When the BPG is at $\Delta V = 0$ for all values of the magnetic field $T_e^g \approx 0.95$ and $T_i^g \approx 0.67$, which is defined by the choice of E_d/E_t. With increasing ΔV, both transparencies decrease and reach zero. In the absence of the magnetic field, it occurs at $\Delta V \approx 40$ V for ions and electrons. This voltage remains

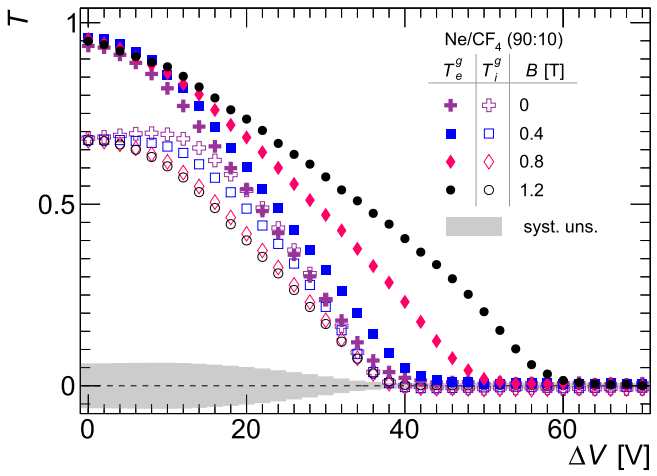

Fig. 5. BPG transparency as a function of ΔV in Ne/CF_4 (90:10) gas mixture at different magnetic field setting. $E_d = 320$ V/cm, $E_t = 480$ V/cm.

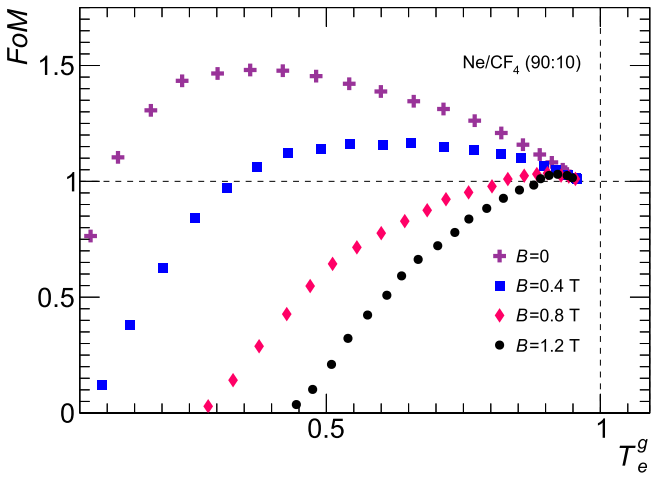

Fig. 6. FoM versus T_e^g for different magnetic field settings.

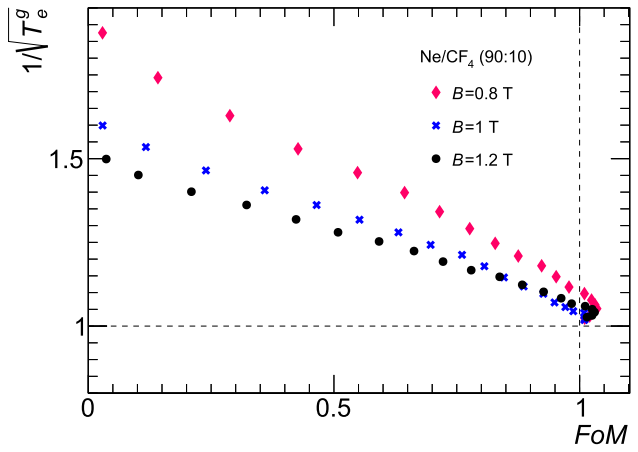

Fig. 7. Dependence of the TPC dE/dx resolution proportional to $1/\sqrt{T_e^g}$ versus FoM at high magnetic fields. Values compare to case of no BPG in the detector, corresponding to point (1,1).

the same for ions also in the presence of the magnetic field although the shape of the T_i^g changes around 10–30 V. This effect is not fully understood. In the presence of a magnetic field, T_e^g behavior changes. It reaches zero at higher voltages with increasing magnetic field. At 1.2 T, T_e^g is still around 0.5 when T_i^g is at zero. Thus, the IBF can be fully shut at the expense of losing approximately half of the primary ionization. In the highest measured field setting, the shape of the T_e^g exhibits a kink at around $\Delta V = 45$ V. Analogous behavior was also seen in [22].

To quantitatively assess the insertion of the BPG element into TPC structure, one can introduce the figure of merit (FoM) that is the ratio of the IBF flowing into the TPC with and without the BPG. The FoM depends on the ratio of the transfer and drift fields $w = E_t/E_d = 1.5$ discussed in Section II-D.2 and can be defined as

$$\mathrm{FoM}(w, \Delta V) = \frac{T_i^m(w, 0)}{T_i^m(1, 0)} \frac{T_i^g(w, \Delta V)}{T_e^g(w, \Delta V)}. \quad (5)$$

The FoM is the product of two terms. The first term results from the discussion of Fig. 4 that higher E_t extracts more ions from the amplification plane of the TPC. Ion current extracted from that plane is characterized in (5) by the ion transparency of the mesh. Thus, the first term is the ratio of T_i^m at the working setting of $w = 1.5$ to that at $w = 1$. The latter corresponds to the setup without the BPG in which the E_d is coupled directly to the mesh.

The second term is the ion transparency T_i^g, divided by the electron transparency T_e^g. The denominator reflects the fact that the loss of primary ionization in BPG must be compensated by increasing the gain in the TPC readout plane, which in turn would generate more ions. The FoM defined by (5) is greater than T_i^g for any ΔV. A TPC with the BPG has a better performance when the FoM takes smaller values.

Fig. 6 showing FoM as a function of T_e^g demonstrates how much the IBF in a TPC can be suppressed by introducing the BPG element into its structure. As follows from (5), point (1,1) indicated in the figure by a crossing of dashed lines corresponds to the case when the BPG is absent in a TPC. All graphs in the figure start in the vicinity of point (1,1) at $\Delta V = 0$. This shows that the BPG at a constant voltage makes little change to the TPC performance in any magnetic field. Increasing ΔV on the BPG wires in a low magnetic field leads to the loss of primary ionization and increase of the IBF, which is seen in the figure from the curves remaining above unity even at low T_e^g. The situation rapidly improves with the increase of the magnetic field, in which the BPG effectively suppresses the IBF while keeping most of the primary ionization.

Suppression of the IBF by the BPG leads to loss of primary electron ionization and thus deteriorates the TPC dE/dx resolution [10]. In the case of the BPG, this effect can be estimated in its leading order as a loss of primary electron statistics. Assuming that the relative loss of the dE/dx resolution is reciprocal to $\sqrt{T_e^g}$, one can plot it versus the FoM as shown in Fig. 7. The curve measured in the $B = 1.2$ T shows that IBF suppression by a factor of 5 is achievable at the expense of 40% deterioration in the dE/dx resolution, and it can be fully suppressed at a cost of 55% of the resolution loss. If such BPG is installed in a TPC with the dE/dx resolution of 10% and IBF of 2%, the resulting performance would be given by the product of these numbers: the TPC and BPG configuration

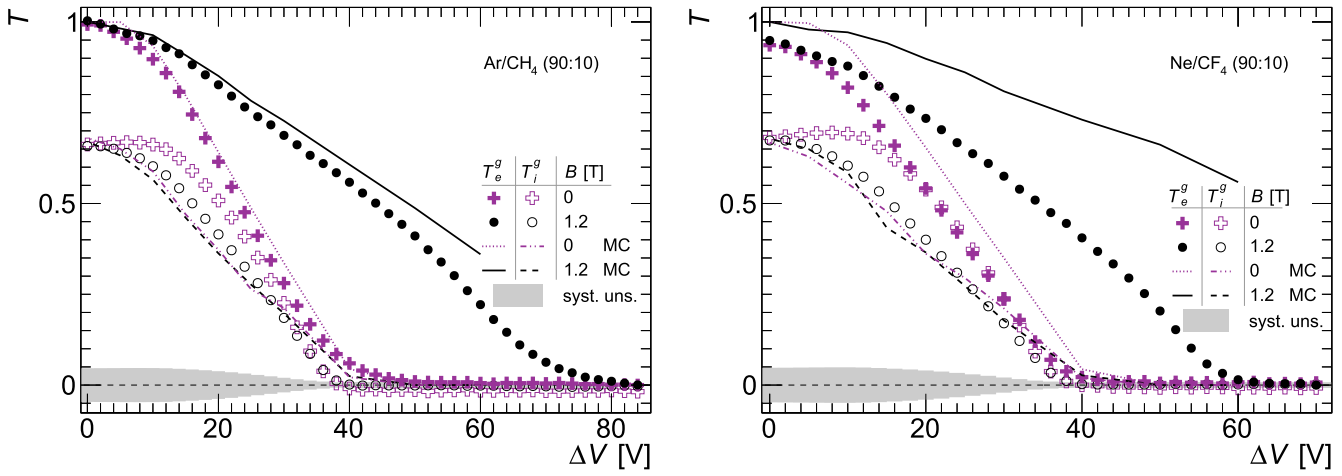

Fig. 8. Transparencies as a function of ΔV compared to the Garfield++ simulation for Ar/CH_4 (90:10) (left) and Ne/CF_4 (90:10) (right) gas mixtures.

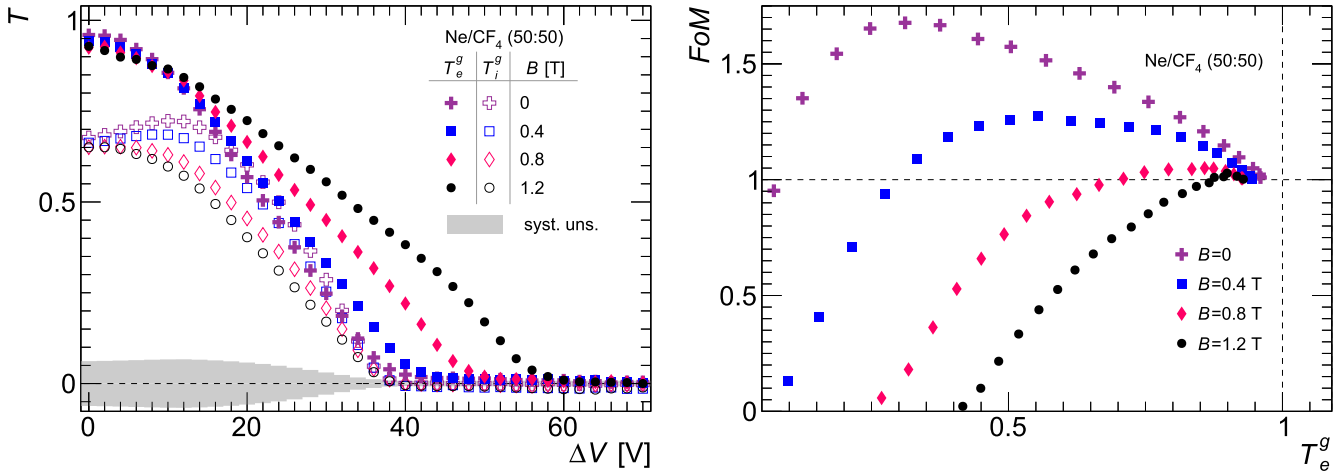

Fig. 9. BPG performance in Ne/CF_4 (50:50) gas mixture at $E_d = 320$ V/cm, $E_t = 480$ V/cm. Left: Transparency as a function of ΔV. Right: FoM versus T_e^g.

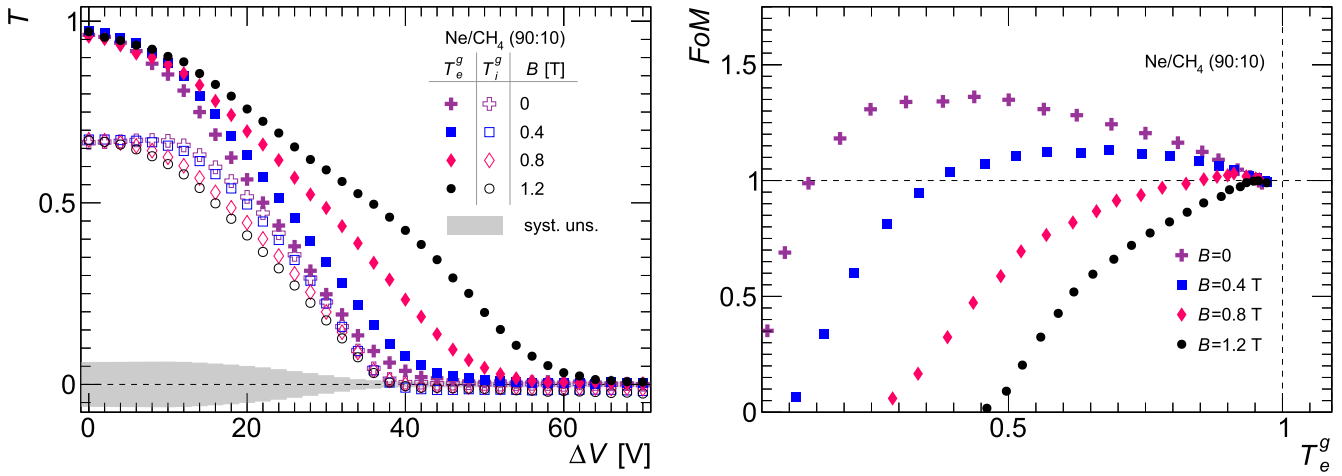

Fig. 10. BPG performance in Ne/CH_4 (90:10) gas mixture at $E_d = 320$ V/cm, $E_t = 480$ V/cm. Left: transparency as a function of ΔV. Right: FoM versus T_e^g.

would have dE/dx resolution of 14% at IBF = 0.4% and no IBF at the dE/dx resolution of 15.5%. The trend of the curve measured at $B = 1.2$ T improves in a higher magnetic field.

Garfield++ toolkit [31] is used to simulate the BPG performance. Gas properties are simulated for Ne/CF_4 (90:10) and Ar/CH_4 (90:10) to reproduce the experimental conditions.

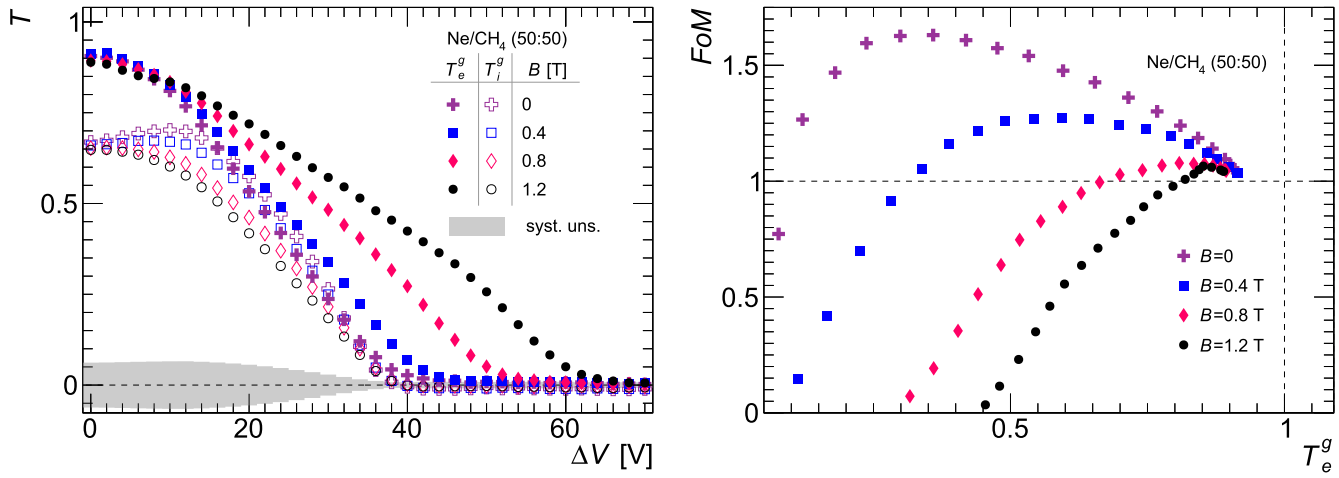

Fig. 11. BPG performance in Ne/CH_4 (50:50) gas mixture at E_d = 320 V/cm, E_t = 480 V/cm. Left: transparency as a function of ΔV. Right: FoM versus T_e^g.

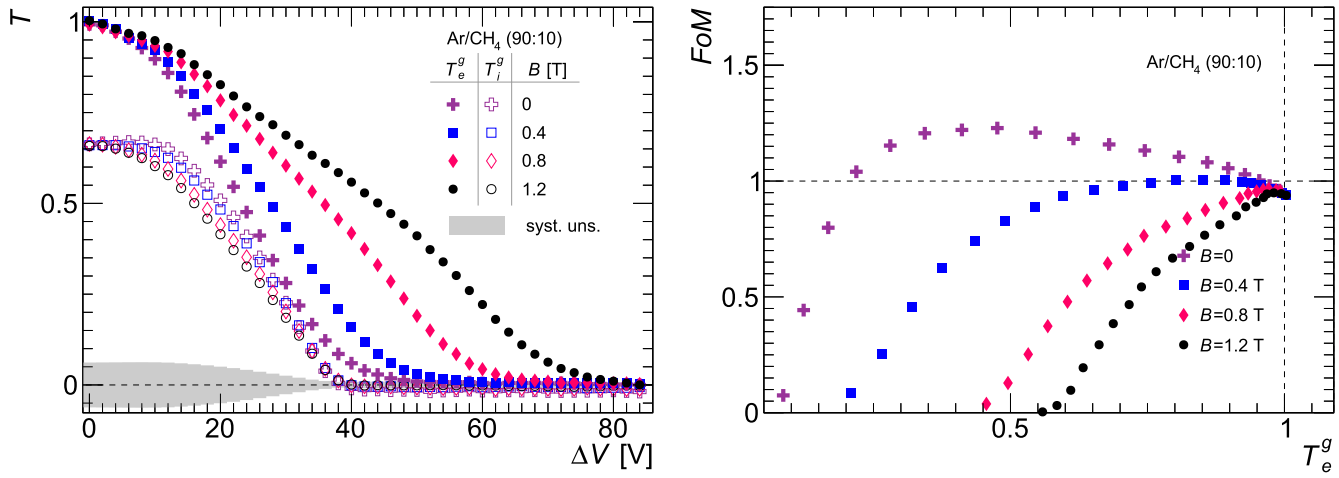

Fig. 12. BPG performance in Ar/CH_4 (90:10) gas mixture at E_d = 320 V/cm, E_t = 480 V/cm. Left: transparency as a function of ΔV. Right: FoM versus T_e^g.

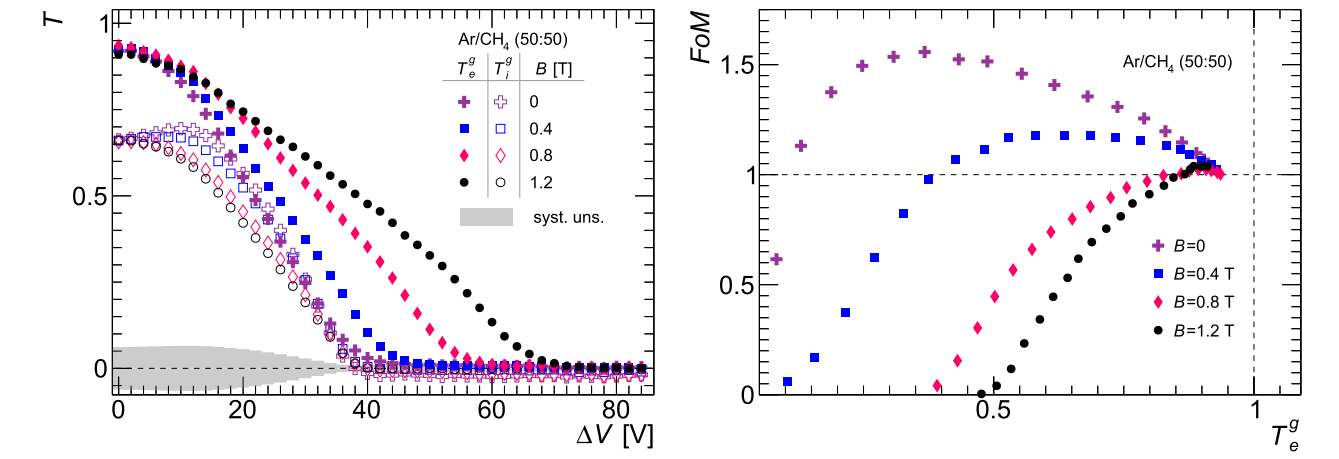

Fig. 13. BPG performance in Ar/CH_4 (50:50) gas mixture at E_d = 320 V/cm, E_t = 480 V/cm. Left: transparency as a function of ΔV. Right: FoM versus T_e^g.

Detector electrodes are modeled using *ComponentAnalyticField* class. Electrons are injected 2 mm above the BPG, and ions originate from the volume of 60 μm in diameter around anode wires. The simulations use *DriftLineRKF* class to calculate the drift lines of the particles. Fig. 8 compares simulation to the measured results for Ar/CH_4 gas mixture

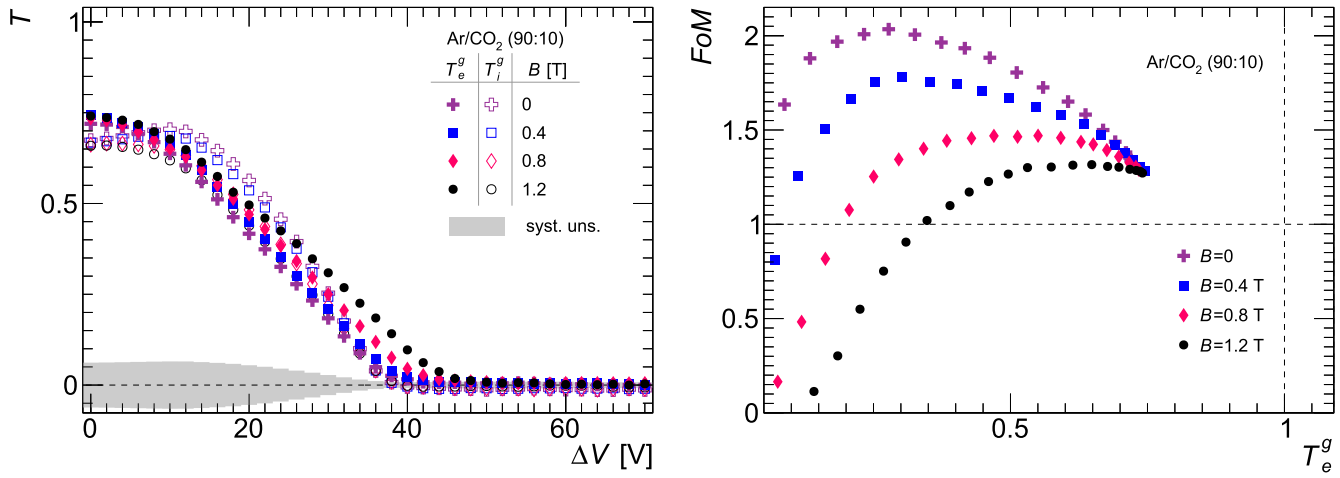

Fig. 14. BPG performance in Ar/CO_2 (90:10) gas mixture at E_d = 320 V/cm, E_t = 480 V/cm. Left: transparency as a function of ΔV. Right: FoM versus T_e^g.

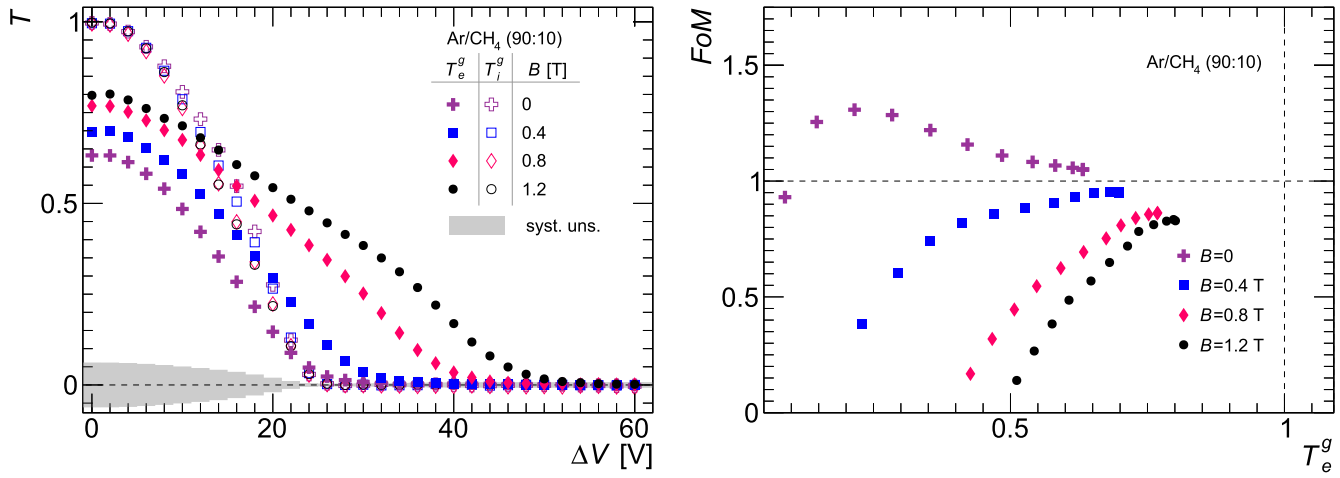

Fig. 15. BPG performance in Ar/CH_4 (90:10) gas mixture at E_d = 320 V/cm, E_t = 160 V/cm. Left: transparency as a function of ΔV. Right: FoM versus T_e^g.

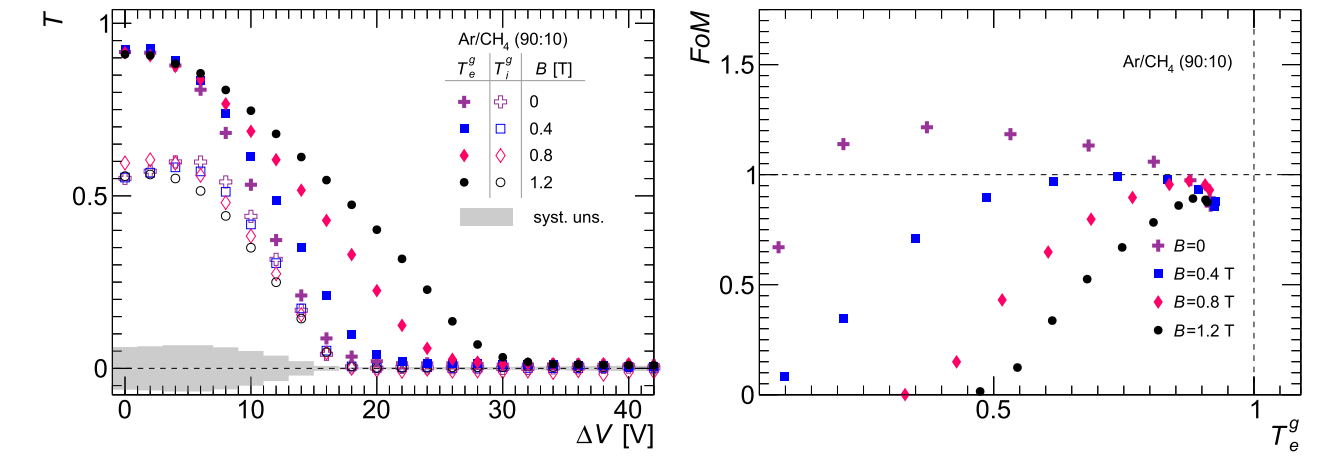

Fig. 16. BPG performance in Ar/CH_4 (90:10) gas mixture at E_d = 140 V/cm, E_t = 210 V/cm. Left: transparency as a function of ΔV. Right: FoM versus T_e^g.

shown in the left panel and Ne/CF_4 shown in the right panel. Comparisons are done for settings without a magnetic field and for B = 1.2 T. In the absence of the magnetic field, the simulation reproduces the electron and ion data within approximately 10%, comparable to the data measurement accuracy. In the presence of a magnetic field, the simulation

curves for ions remain the same, whereas the data shows different shapes. Nevertheless, the point where the T_i reaches zero is well reproduced by the simulation. For Ar/CH_4 gas mixture, the simulation curve for T_e agrees with the data reasonably well but for Ne/CF_4 it shows the significant deviation.

V. Discussion and Conclusion

The experimental setup built at the Weizmann Institute of Science is used to measure electron and ion transparencies of a bipolar wire grid operated in a magnetic field in passive mode. Studies are made in Ne-based and Ar-based gas mixtures using CH_4, CF_4, and CO_2 as quenchers. The results for Ar/CH_4 (90:10) are qualitatively consistent with the measurements published in [22].

The performance of the bipolar grid is evaluated in terms of transparencies to electron and ion currents traversing it from above and from below, respectively. Since the transparencies of the grid strongly depend on the electric fields coupled to it (Fig. 12 versus 15), most measurements are performed in configuration with electric fields 320 and 480 V/cm above and below the grid, respectively. This configuration is chosen to facilitate comparisons between different gas mixtures. As a result, several common features can be seen in all measurements (Figs. 5, 6, and 9–14). Without voltage bias on the grid wires, grid transparency to ions is about 70% and grid transparency to electrons is above 90% in all gas mixtures, except in Ar/CO_2 (Fig. 14), where it is close to the ion transparency. Transparency values for electrons and ions measured at zero bias in the main field configuration do not depend on the strength of the magnetic field. Increasing voltage bias on the wires to ± 40 V in all gases brings the ion transparency to zero even in the strongest measured magnetic field of 1.2 T. At 1-mm pitch between the grid wires, this bias corresponds to an electric field of approximately 800 V/cm, twice the average of the coupled fields. An empirical estimate that the field inside the grid required to zero out the ion current through it shall be twice the field coupled to the grid also holds for other field configurations measured in this study (Figs. 15 and 16). The shape of the curve for ion transparency shows weak dependence on the magnetic field, although the nature of the elevation that develops in the 10–30 V region in stronger magnetic fields is not clear. Garfield-based simulations well reproduce the grid transparency to ions but show no shape dependence on the magnetic field.

Grid transparency to electrons is sensitive to the magnetic field and the required voltage bias to zero out the electron current increases in higher magnetic field by nearly a factor of 2 compared to ions (Figs. 10 and 12). At ± 40 V required to stop the ion flow, in 1.2 T field the grid retains 45%–60% transparency to electrons. The simulations reproduce the behavior of grid transparency to electrons in the absence of a magnetic field, but in some gases, the simulations show significant deviations from the measured curves when the magnetic field is present (Fig. 8).

To quantitatively evaluate the impact of the grid element in the structure of the TPC, a figure of merit is introduced as explained in Section IV. Its smaller values correspond to better performance of the TPC with the grid in suppressing positive IBF. A grid without voltage bias on its wires makes almost no impact on the TPC performance in any magnetic field, except in Ar/CO_2 gas mixture. Although this may be seen as a trivial statement, the measurements show if a grid plane is built in a TPC for the purpose to decouple drift and amplification regions, it makes almost no impact on the TPC performance (Figs. 6, and 9–14).

With the voltage bias on the wires, the grid performance strongly depends on the magnetic field. The effect of the grid in gas mixtures with small Lorentz angle using CO_2 as a quencher is insignificant, but it drastically improves in gases with larger Lorentz angles, such as the mixtures with CF_4 and CH_4. Between these two gases, CH_4 shows slightly better results (Fig. 10 versus 6, and Fig. 11 versus 9). The results somewhat improve in the mixtures with a lower concentration of the quenching gas (Fig. 10 versus 11, Fig. 6 versus 9, and Fig. 12 versus 13). For the same quencher, Ar-based mixtures show better results compared to Ne-based mixtures (Fig. 12 versus 10, and Fig. 13 versus 11).

Although the results measured in this study are qualitatively consistent with the expectations coming from the theory of electrons and ions drift in gases [21], [25], the quantitative comparison shows significant deviations from the measured data, especially for electrons. Simulations based on Garfield++ toolkit are not sufficiently accurate in describing measurements in some gases (Fig. 8).

To get more insights into this problem, measurement were also done in other field configuration (Figs. 15 and 16). Field change results in different behavior seen in curves, which, in some cases, are consistent with expectations determined by the field changes. A surprising result is that although in Ar/CH_4 the Lorentz angle in lower electric field is expected to almost double [32] compared to the main setting, the measurements show that it results into small reduction of transparency to electrons (Figs. 12 versus 16).

Although some of the measured effects are not reproduced by simulation, results reported in the article demonstrate that a passive bipolar grid operated in a magnetic field above 1 T can be used as an effective instrument to suppress the IBF in TPCs.

Appendix

Measurements of T_e^g and T_i^g versus ΔV and FoM versus T_e^g for the BPG in different gases at zero magnetic fields and 0.4, 0.8, and 1.2 T. Measurements for Ne/CF_4 (90:10) gas mixture are given in Figs. 5 and 6. To preserve the clarity of the plots, the dependence of systematic uncertainty on ΔV is shown as a band around zero. It has to be taken as the uncertainty estimator for individual curves shown in figures. The systematic uncertainties are described in Section III.

Acknowledgment

The authors would like to express gratitude to Prof. Amos Breskin and Dr. Arindam Roy of the Weizmann Institute for fruitful discussions and help. The authors are thankful to the High-Energy group at the Weizmann Institute working on the ATLAS experiment for their help in making parts of the setup.

The authors would like to thank the group of Prof. Mirko Planinić from the University of Zagreb for help with setting up floating picoammerts and the reliable performance of their devices during the measurements. Special thanks are to the Physics Core Facility group of the Weizmann Institute for their constant support during the experiment.

REFERENCES

[1] D. Nygren. (1974). *Proposal to Investigate the Feasibility of a Novel Concept in Particle Detection*. [Online]. Available: https://inspirehep.net/literature/1365360

[2] H. Aihara *et al.*, "Spatial resolution of the PEP-4 time projection chamber," *IEEE Trans. Nucl. Sci.*, vol. NS-30, no. 1, pp. 76–81, Feb. 1983.

[3] T. Kamae *et al.*, "The Topaz time projection chamber," *Nucl. Instrum. Meth. Phys. Res. A, Accel. Spectrom. Detect. Assoc. Equip.*, vol. 252, nos. 2–3, pp. 423–430, 1986.

[4] C. Brand *et al.*, "The Delphi time projection chamber," *Nucl. Instrum. Meth. Phys. Res. A, Accel. Spectrom. Detect. Assoc. Equip.*, vol. 283, no. 3, pp. 567–572, 1989.

[5] W. Atwood *et al.*, "Performance of the Aleph time projection chamber," *Nucl. Instrum. Meth. Phys. Res. A, Accel. Spectrom. Detect. Assoc. Equip.*, vol. 306, no. 3, pp. 446–458, 1991.

[6] M. Fuchs, "Very high multiplicity tracking in heavy ion collisions with the NA49 time projection chambers (TPCs)," *Nucl. Instrum. Meth. Phys. Res. A, Accel. Spectrom. Detect. Assoc. Equip.*, vol. 367, nos. 1–3, pp. 394–397, Dec. 1995.

[7] M. Anderson *et al.*, "The STAR time projection chamber: A unique tool for studying high multiplicity events at RHIC," *Nucl. Instrum. Meth. Phys. Res. A, Accel. Spectrom. Detect. Assoc. Equip.*, vol. 499, nos. 2–3, pp. 659–678, Mar. 2003.

[8] J. Alme *et al.*, "The ALICE TPC, a large 3-dimensional tracking device with fast readout for ultra-high multiplicity events," *Nucl. Instrum. Meth. Phys. Res. A, Accel. Spectrom. Detect. Assoc. Equip.*, vol. 622, no. 1, pp. 316–367, Oct. 2010.

[9] M. Ball *et al.*, "Technical design study for the PANDA time projection chamber," 2012, *arXiv:1207.0013*. [Online]. Available: http://arxiv.org/abs/1207.0013

[10] B. Abelev and Alice Collaboration, "Upgrade of the ALICE experiment: Letter of intent," *J. Phys. G. Nucl. Part. Phys.*, vol. 41, no. 8, 2014, Art. no. 087001.

[11] P. Colas, I. Giomataris, and V. Lepeltier, "Ion backflow in the micromegas TPC for the future linear collider," *Nucl. Instrum. Meth. Phys. Res. A, Accel. Spectrom. Detect. Assoc. Equip.*, vol. 535, nos. 1–2, pp. 226–230, Dec. 2004.

[12] F. Sauli, L. Ropelewski, and P. Everaerts, "Ion feedback suppression in time projection chambers," *Nucl. Instrum. Meth. Phys. Res. A, Accel. Spectrom. Detect. Assoc. Equip.*, vol. 560, no. 2, pp. 269–277, May 2006.

[13] S. Kappler *et al.*, "A GEM-TPC prototype with low-noise highly integrated front-end electronics for linear collider studies," *IEEE Trans. Nucl. Sci.*, vol. 51, no. 3, pp. 1039–1043, Jun. 2004.

[14] A. Bondar, A. Buzulutskov, L. Shekhtman, and A. Vasiljev, "Study of ion feedback in multi-GEM structures," *Nucl. Instrum. Meth. Phys. Res. A, Accel. Spectrom. Detect. Assoc. Equip.*, vol. 496, nos. 2–3, pp. 325–332, Jan. 2003.

[15] S. Blatt *et al.*, "Charge transfer of GEM structures in high magnetic fields," *Nucl. Phys. B-Proc. Supplements*, vol. 150, pp. 155–158, Jan. 2006.

[16] R. Chechik *et al.*, "Recent investigations of cascaded GEM and MHSP detectors," *IEEE Trans. Nucl. Sci.*, vol. 51, no. 5, pp. 2097–2103, Oct. 2004.

[17] A. S. Conceicao, J. A. Mir, J. M. Maia, and J. M. F. D. Santos, "Ion backflow suppression in GEM-MIGAS," *IEEE Trans. Nucl. Sci.*, vol. 57, no. 6, pp. 3753–3759, Dec. 2010.

[18] F. V. Böhmer *et al.*, "Simulation of space-charge effects in an ungated GEM-based TPC," *Nucl. Instrum. Meth. Phys. Res. A, Accel. Spectrom. Detect. Assoc. Equip.*, vol. 719, pp. 101–108, Aug. 2013.

[19] S. Aiola *et al.*, "Combination of two gas electron multipliers and a micromegas as gain elements for a time projection chamber," *Nucl. Instrum. Meth. Phys. Res. A, Accel. Spectrom. Detect. Assoc. Equip.*, vol. 834, pp. 149–157, Oct. 2016.

[20] S. Wang *et al.*, "Studies on ion back-flow of time projection chamber based on GEM and anode wire grid," *Nucl. Instrum. Meth. Phys. Res. A, Accel. Spectrom. Detect. Assoc. Equip.*, vol. 940, pp. 410–416, Oct. 2019.

[21] H. Hilke, "Time projection chambers," *Rep. Prog. Phys.*, vol. 73, no. 11, Oct. 2010, Art. no. 116201.

[22] S. Amendolia *et al.*, "Influence of the magnetic field on the gating of a time projection chamber," *Nucl. Instrum. Meth. Phys. Res. A, Accel. Spectrom. Detect. Assoc. Equip.*, vol. 234, no. 1, pp. 47–53, 1985.

[23] S. Amendolia *et al.*, "Gating in the ALEPH time projection chamber," *Nucl. Instrum. Meth. Phys. Res. A, Accel. Spectrom. Detect. Assoc. Equip.*, vol. 252, nos. 2–3, pp. 403–406, 1986.

[24] J. Kent. (1984). *Positive Ion Suppression With Untriggered TPC*. [Online]. Available: https://inspirehep.net/literature/15653

[25] F. Sauli, Ed., *Instrumentation in High Energy Physics*, vol. 9, 2nd ed. Singapore: World Scientific, 1992.

[26] W. Blum, W. Riegler, and L. Rolandi, *Particle Detection With Drift Chambers*, 2nd ed. Berlin, Germany: Springer, 2008.

[27] A. Adare *et al.*, "An upgrade proposal from the PHENIX collaboration," *arXiv:1501.06197*, 2015. [Online]. Available: https://arxiv.org/abs/1501.06197.

[28] sPHENIX Collaboration. (2015). *sPHENIX Preconceptual Design Report*. [Online]. Available: https://inspirehep.net/literature/1500630

[29] A. Utrobicic, M. Kovacic, F. Erhardt, N. Poljak, and M. Planinic, "A floating multi-channel picoammeter for micropattern gaseous detector current monitoring," *Nucl. Instrum. Meth. Phys. Res. A, Accel. Spectrom. Detect. Assoc. Equip.*, vol. 801, pp. 21–26, Nov. 2015.

[30] H. Wieman *et al.*, "STAR TPC at RHIC," *IEEE Trans. Nucl. Sci.*, vol. 44, no. 3, pp. 671–678, Jun. 1997.

[31] (2020). *Garfield++ Webpage*. [Online]. Available: http://cern.ch/garfieldpp

[32] X. Bittl *et al.*, "Diffusion and drift studies of ar-DME/CO_2/CH_4 gas mixtures for a radial TPC in the E $\perp$ B field," *Nucl. Instrum. Meth. Phys. Res. A, Accel. Spectrom. Detect. Assoc. Equip.*, vol. 398, nos. 2–3, pp. 249–264, 1997.